Monthly Notices
of the
ROYAL ASTRONOMICAL SOCIETY

MNRAS **483,** 1970–1979 (2019)
Advance Access publication 2018 November 29

doi:10.1093/mnras/sty3230

K2-161b: a low-density super-Neptune on an eccentric orbit

R. Brahm,[1,2,3]★† N. Espinoza,[4]★‡ M. Rabus,[1,4] A. Jordán,[2,3]★ M. R. Díaz,[5] F. Rojas,[2] M. Vučković,[6] A. Zapata,[1] C. Cortés,[3,7] H. Drass,[1,3] J. S. Jenkins,[5] R. Lachaume,[1,4] B. Pantoja,[5] P. Sarkis,[4] M. G. Soto,[5] S. Vasquez,[8] Th. Henning[4] and M. I. Jones[9]

[1]*Center of Astro-Engineering UC, Pontificia Universidad Católica de Chile, Av. Vicuña Mackenna 4860, 7820436 Macul, Santiago, Chile*
[2]*Instituto de Astrofísica, Facultad de Física, Pontificia Universidad Católica de Chile, Av. Vicuña Mackenna 4860, 7820436 Macul, Santiago, Chile*
[3]*Millennium Institute of Astrophysics, Santiago, Chile*
[4]*Max-Planck-Institut für Astronomie, Königstuhl 17, D-69117 Heidelberg, Germany*
[5]*Departamento de Astronomía, Universidad de Chile, Camino El Observatorio 1515, Las Condes, Santiago, Chile*
[6]*Instituto de Física y Astronomía, Universidad de Vaparaíso, Casilla 5030, Valparaíso, Chile*
[7]*Departamento de Física, Facultad de Ciencias Básicas, Universidad Metropolitana de la Educación, Av. José Pedro Alessandri 774, 7760197, Nuñoa, Santiago, Chile*
[8]*Museo Interactivo Mirador, Dirección de Educación, Av. Punta Arenas 6711, La Granja, Santiago, Chile*
[9]*European Southern Observatory, Casilla 19001, Santiago, Chile*

Accepted 2018 November 26. Received 2018 November 21; in original form 2018 June 11

ABSTRACT

We report the discovery of K2-161b, which was first identified as a planetary candidate from *Kepler* K2 photometry of Campaign 14, and whose planetary nature and orbital parameters were then confirmed with precision radial velocities. K2-161b is half as massive as Saturn ($M_P = 0.179 \pm 0.021\,M_J$), and has a radius of $R_P = 0.840 \pm 0.011\,R_J$, which translates into a bulk density of $\rho_P = 0.37 \pm 0.05\,g\,cm^{-3}$. K2-161b transits its slightly evolved G-type host star ($M_\star = 1.105 \pm 0.019\,M_\odot$, $R_\star = 1.669 \pm 0.022\,R_\odot$) every 11.633 64 ± 0.000 10 d and presents a significantly eccentric orbit ($e = 0.420 \pm 0.034$). We estimate a relatively short circularization time-scale of 1.8 Gyr for the planet, but given the advanced age of the system we expect the planet to be engulfed by its evolving host star in ∼1 Gyr before the orbit circularizes. The low density of the planet coupled to the brightness of the host star ($J = 9.4$) makes this system one of the best candidates known to date in the super-Neptune regime for atmospheric characterization via transmission spectroscopy, and to further study the transition region between ice and gas giant planets.

Key words: techniques: photometric – techniques: radial velocities – planets and satellites: fundamental parameters – stars: fundamental parameters – stars: individual: K2-161.

1 INTRODUCTION

Transiting planets in the transition region between ice- and gas-giants (super-Neptunes, e.g. Bakos et al. 2015) are fundamental objects for constraining planet formation theories, particularly regarding the runaway accretion of the gaseous envelope (Ida & Lin 2004; Mordasini, Alibert & Benz 2009). The physical parameters (mass and radius) of these planets can be compared to theoretical models in order to infer their internal composition (heavy element content), which can be linked to the observed star–planet system properties and predicted formation conditions (Thorngren et al. 2016). In addition, the detection of molecules in the atmospheres of these planets via transmission spectroscopy can be connected to different orbital distances at which the formation of the planet or accretion of the envelope took place (Mordasini et al. 2016; Espinoza et al. 2017b). Additionally, detailed characterization of the orbital parameters of these systems can deliver clues about their formation and/or migration histories (Dawson & Murray-Clay 2013; Petrovich & Tremaine 2016).

None the less, super-Neptunes are among the least studied type of transiting planets to date, due to the low number of detected systems around bright stars. The photometric precision of ground-based surveys is barely enough to discover planets slightly smaller than Jupiter (Bakos et al. 2010; Brahm et al. 2018a; Demangeon et al. 2018), and most of the Kepler systems found in the super-Neptune region are too faint for determining their masses via precision radial

★ E-mail: rbrahm@gmail.com (RB); espinoza@mpia-hd.mpg.de (NE); ajordan@astro.puc.cl (AJ)
† Fondecyt Fellow.
‡ Bernoulli Fellow.

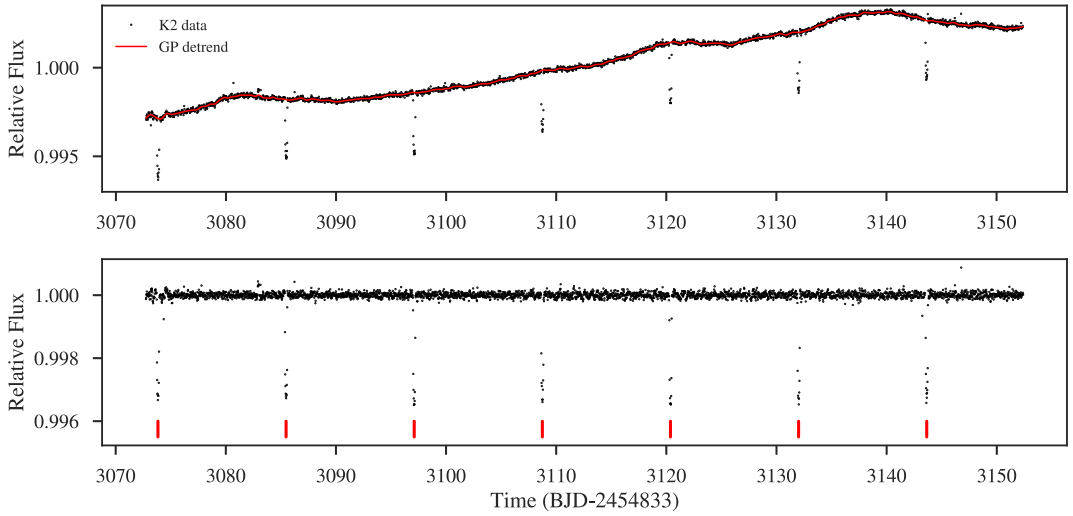

Figure 1. K2 light curve for K2-161 before (top panel) and after (bottom panel) applying the de-trending model.

velocities (e.g. Borucki et al. 2011). Therefore, most of what we know about these planets has come from statistical studies of Kepler validated systems (e.g. Buchhave et al. 2012; Fulton et al. 2017), and ground-based radial velocity surveys (e.g. Jenkins et al. 2017; Udry et al. 2017). This picture has started to change thanks to the *Kepler* K2 mission (Howell et al. 2014), which has been able to monitor a significant number of bright stars with very high photometric precision, resulting in the discoveries and dynamical characterization of several of these types of planets (e.g. Barragán et al. 2016; Van Eylen et al. 2016; Dressing et al. 2018). We expect this number to grow significantly once the first light curves from the TESS mission become available (Ricker et al. 2015; Barclay, Pepper & Quintana 2018).

In this study, we present the discovery of a warm super-Neptune planet that transits its host star, and presents one of the largest eccentricities known for short period planets in this mass range. This discovery was performed in the context of the K2CL collaboration, which uses spectroscopic facilities located in Chile to confirm and characterize transiting planets from K2 (Brahm et al. 2016; Espinoza et al. 2017a; Jones et al. 2017; Brahm et al. 2018b; Giles et al. 2018; Soto et al. 2018). The structure of the paper is as follows. In Section 2, we present the photometric and spectroscopic observations that allowed the discovery of K2-161b, in Section 3 we derive the planetary and stellar parameters, and we discuss our findings in Section 4.

2 OBSERVATIONS

2.1 Kepler K2

Observations of field 14 of K2 mission (RA = $10^{h}42^{m}44^{s}$, DEC = $+06^{o}51'06''$) were performed between May and August of 2017, and were released to the community on November of the same year. The photometric data for all targets of this campaign was reduced from pixel-level products to photometric light curves using the EVEREST algorithm (Luger et al. 2016, 2017), where long-term trends in the data were corrected with a Gaussian-process regression. Specifically, we use the basic kernel presented in equation 17 by Luger et al. (2017) (a Matérn-3/2 plus white noise kernel) with the following values for the hyper parameters: $\sigma = 51.59\,e^{-}s^{-1}$, $\alpha = 60\,024.56\,e^{-}s^{-1}$, and $\tau = 100$ d. As in previous K2 campaigns, the transiting planet detection was performed by using the Box-fitting Least Squares algorithm (Kovács, Zucker & Mazeh 2002) on the processed light curves. With this procedure we identified 41 planetary candidates, among which K2-161 with an estimated period of 11.6 d, was catalogued as high priority due to the brightness of the star and its clean box-shaped transits with depths of ≈3000 ppm (see Fig. 1).

2.2 Spectroscopic observation

Our spectroscopic follow-up campaign consists primarily in the use of four stabilized echelle spectrographs installed at the ESO La Silla Observatory in Chile. We use the FIDEOS spectrograph installed on the ESO 1 m telescope (Vanzi et al. 2018) and the Coralie spectrograph Queloz et al. (2000) on the 1.2 m-Euler/Swiss telescope for performing an initial characterization of the host star in order to reject false positives. Particularly for the case of K2-161, we obtained three Coralie spectra on three different nights between January and March of 2018. Observations were performed with the simultaneous calibration mode (Baranne et al. 1996) in which the comparison fibre is illuminated with a Fabry–Pérot etalon (Cersullo et al. 2017) in order to trace the instrumental drift produced by environmental changes during the observation. The adopted exposure times ranged between 1500 and 1800 s, and achieved a signal-to-noise ratio of 40–50 per resolution element. These three spectra were reduced and processed with the automated CERES pipeline (Jordán et al. 2014; Brahm, Jordán & Espinoza 2017a), which performs the optimal extraction and wavelength calibration, and delivers precision radial velocities, bisector span (BIS) measurements, and an estimation of the atmospheric parameters. No additional stellar components were identified in the spectra, and no large amplitude velocity variations were observed, which could have been originated by an eclipsing stellar mass companion.

After this initial characterization, more powerful facilities are required to determine the mass and orbital parameters of the hypothetical planetary companion. We acquired 43 spectra with FEROS (Kaufer et al. 1999) installed on the MPG2.2m telescope and 12 spectra with HARPS (Mayor et al. 2003) installed on the ESO3.6m telescope. These observations were performed between March and

Table 1. Summary of spectroscopic observations for K2-161.

Instrument	UT date(s)	N spec.	Resolution	S/N range (≈5100 Å)	RV precision (m s^{-1})
Coralie/1.2m Euler/Swiss	2018 Jan–Mar	3	60 000	40–51	10
FEROS/2.2m MPG	2018 Jan–May	43	50 000	106–167	7
HARPS/3.6m ESO	2018 Jan–May	12	115 000	36–50	2

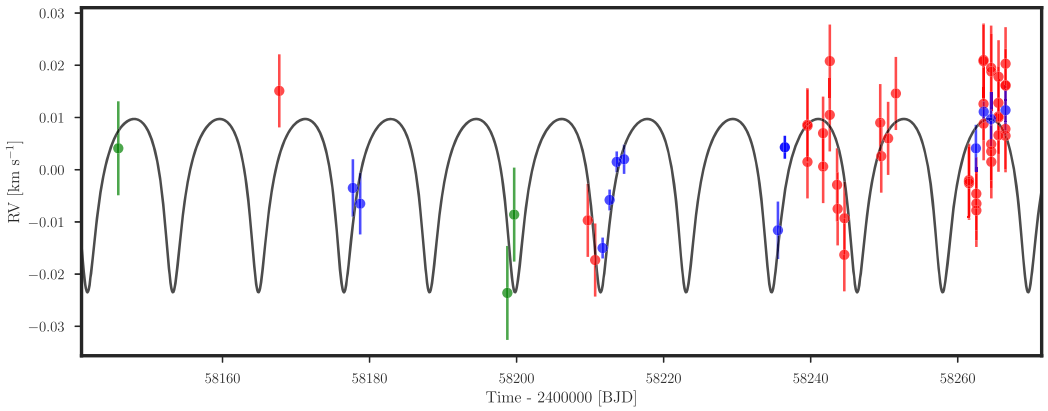

Figure 2. RV curve obtained with Coralie (green), FEROS (red), and HARPS (blue). The black line corresponds to the Keplerian model with the posterior parameters found in Section 3.

May of 2018. In the case of the FEROS observations, the instrumental drift during the science observations was monitored with the secondary fibre which was illuminated by a ThAr + Ne lamp. No instrumental drift was monitored during the HARPS observations because the stability of this instrument is significantly higher than the amplitude in radial velocity that we intend to measure. The comparison fibre was pointed to the background sky. Table 1 summarizes the general properties of these observations. The data from both instruments was processed through the CERES package in order to obtain precision radial velocities and BIS measurements from the raw science images. These measurements are presented in Table A1, and the radial velocity (RV) curve is shown in Fig. 2.

The velocities present a periodic variation that matches that of the transit signal. In fact, a blind and wide-parameter search performed by the EMPEROR[1] code (Jenkins & Peña in preparation) on the RVs uncovered a statistically significant signal matching the properties indicated by the transit data, providing independent confirmation of the reality of the planet. The relatively low amplitude of the variation implies a sub-Jovian mass for the orbital companion, while the shape of the variation shows that the orbit is significantly non-circular. Additionally, a scatter plot of the radial velocities and BIS values is displayed in Fig. 3. No significant correlation is observed, which further reduces the probability that the system corresponds to a blended eclipsing binary or that the radial velocity signal is produced by stellar activity. In concrete terms, the median *Pearson* coefficient value between RVs and BIS is −0.15 with a 95 per cent confidence interval between −0.44 and 0.24, representing no statistically significant correlation. Finally, the stellar atmospheric parameters reported by CERES in the case of the three instruments were consistent with those of a sub-giant star ($T_{\rm eff} \approx 5400$ K, $\log g \approx 3.8$, [Fe/H] ≈ 0.2).

[1] https://github.com/ReddTea/astroEMPEROR

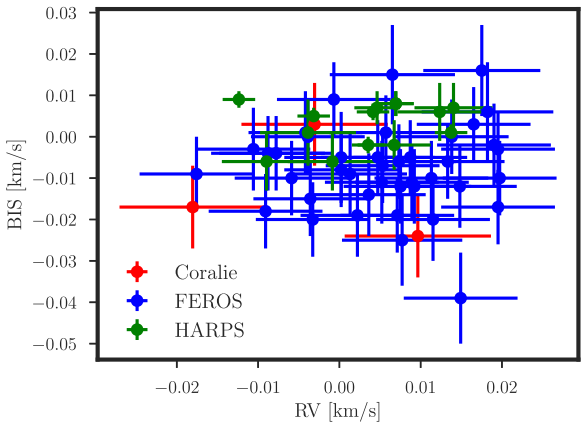

Figure 3. RV versus BIS scatter plot using data from our spectroscopic observations of K2-161. No significant correlation was found.

2.3 GAIA

K2-161 was also observed by GAIA. According to GAIA DR2 (Gaia Collaboration et al. 2018), no companions were identified inside the aperture of the K2 photometry (≈20 arcsec), which could be affecting the transit depth measured with the *Kepler* telescope (Ciardi et al. 2015). Additionally, the reported radial velocity (3.28 ± 0.52 km s^{-1}) and $T_{\rm eff}$ (5288 ± 120 K) values are consistent with those obtained through our spectroscopic follow-up observations. A parallax of $\pi = 4.660 \pm 0.043$ mas is reported, which we use to determine the stellar properties as described in Section 3.

3 ANALYSIS

3.1 Stellar parameters

For computing the physical parameters of K2-161, we follow an iterative procedure that consists in the following steps:

(i) Determination of the stellar atmospheric parameters ($T_{\rm eff}$, $\log g$, [Fe/H], $v \sin i$) from high-resolution spectra.
(ii) Determination of the stellar radius ($R_\star$) and extinction factor (A_V) from the GAIA parallax and available photometry.
(iii) Determination of the stellar mass ($M_\star$) and age by comparing the obtained stellar radius and $T_{\rm eff}$ with theoretical evolutionary tracks.
(iv) Computation of a new $\log g$ value from $R_\star$ and $M_\star$, which is used as a fixed parameter in the following iteration.

Particularly for the case of K2-161 only two iterations were required. As a convergence criteria, we simply check that the $\log g$ value obtained from the fit to the isochrones is consistent at the 1σ level with the value previously obtained from the spectroscopic analysis.

We obtained the atmospheric parameters with the `ZASPE` code (Brahm et al. 2015, 2017b) from the co-added HARPS spectra. `ZASPE` determines $T_{\rm eff}$, $\log g$, [Fe/H], and $v \sin i$ by comparing the observed spectrum to synthetic ones in the spectral regions most sensitive to changes in those parameters. Additionally, reliable uncertainties are obtained from the data by performing Monte Carlo simulations that take into account the systematic mismatches between data and models. Using this procedure, we obtained the following parameters for the first iteration: $T_{\rm eff} = 5532 \pm 70$ K, $\log g = 4.04 \pm 0.127$ dex, [Fe/H] $= 0.26 \pm 0.04$ dex, and $v \sin i = 3.44 \pm 0.43$ km s^{-1}, which were close to those obtained in the final iteration: $T_{\rm eff} = 5513 \pm 51$ K, $\log g = 4.032 \pm 0.015$ dex, [Fe/H] $= 0.26 \pm 0.03$ dex, and $v \sin i = 3.7 \pm 0.17$ km s^{-1}. Additionally, we performed an independent estimation of the stellar atmospheric parameters using the `SPECIES` (Soto & Jenkins 2018) finding consistent results at the 1σ level to those computed with `ZASPE`.

For the second step, we used the `BT-Settl-CIFIST` spectral models from Baraffe et al. (2015), which were interpolated to generate a synthetic spectral energy distribution (SED) consistent with the atmospheric parameters of K2-161. We then integrated the SED in different spectral regions to generate synthetic magnitudes that were weighted by the corresponding transmission functions of the passband filters. The synthetic SED along with the observed flux density in the different filters are plotted in Fig. 4.

Following the same procedure described in Brahm et al. (2018b), these synthetic magnitudes were used to infer the stellar radius ($R_\star$) and the extinction factor (A_V) by comparing them to the observed magnitudes after applying a correction of the dilution of the stellar flux due to the distance computed from the GAIA parallax. We used the `emcee` `Python` package (Foreman-Mackey et al. 2013) to sample the posterior distribution of $R_\star$ and A_V. We also repeated this process for different values of $T_{\rm eff}$ sampled from a Gaussian distribution, finding that the uncertainty in the final stellar radius is dominated by the uncertainty in $T_{\rm eff}$. The stellar radius obtained in the last iteration was of $R_\star = 1.669 \pm 0.022$ R$_\odot$, which includes the error budget provided by the uncertainty in $T_{\rm eff}$.

For the third step, we used the Yonsei-Yale isochrones (Yi et al. 2001), which were interpolated to the metallicity found with `ZASPE`. We used the `emcee` package to explore the posterior distribution of the stellar masses and ages that generate stellar radii and effective temperatures consistent with the values found in the previous steps. Fig. 5 shows different isochrones in the $T_{\rm eff}$–$R_\star$ plane, with the value for K2-161 indicated in blue. The final parameters obtained for K2-161 are listed in Table 2. We found that K2-161 is a G-type star with a mass of M$_\star = 1.105 \pm 0.019$ M$_\odot$, that has just recently started to depart from the main sequence at an age of 8.5 ± 0.5 Gyr.

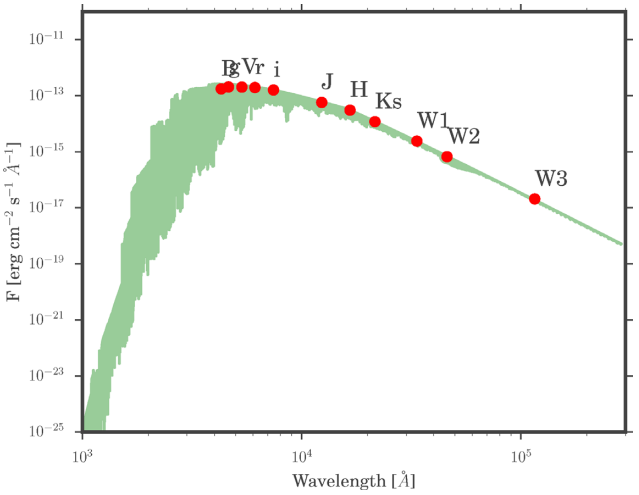

Figure 4. SED of the `BT-Settl-CIFIST` model for the atmospheric parameters of K2-161. The red circles correspond to the observed flux densities for the different passband filters are identified as red circles.

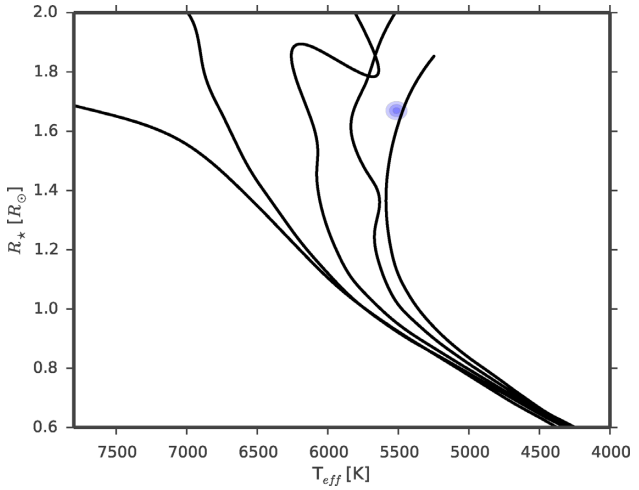

Figure 5. Yonsei-Yale isochrones for the metallicity of K2-161 in the $T_{\rm eff}$–$R_\star$ plane. From left to right the isochrones correspond to 0.1, 1, 3, 6, 9 Gyr. The position of K2-161 in this plane is shown in blue, where the three different intensities represent the 1σ, 2σ, and 3σ contours.

3.2 Global modelling

In order to determine the orbital and transit parameters of the K2-161b system, we performed a joint analysis of the de-trended photometry of the *Kepler* telescope and follow-up radial velocities. As in previous planet discoveries of the K2CL collaboration, we used the `exonailer` code which is described in detail in Espinoza et al. (2016). Briefly, we model the transit light curves using the `batman` package (Kreidberg 2015) by taking into account the smearing effect of the transit shape produced by the long cadence of K2 (Kipping 2010). To avoid systematic biases in the

Table 2. Stellar properties and parameters for K2-161.

Parameter	Value	Method/source
Names	K2-161, EPIC 201498078	–
RA	$10^{h}52^{m}07.78^{s}$	–
DEC	$00^{o}29'36.07''$	–
Parallax (mas)	4.660 ± 0.042	GAIA
K_p (mag)	10.451	EPIC
B (mag)	11.561 ± 0.086	APASS
g (mag)	10.979 ± 0.010	APASS
V (mag)	10.612 ± 0.059	APASS
r (mag)	10.402 ± 0.020	APASS
i (mag)	10.226 ± 0.020	APASS
J (mag)	9.337 ± 0.030	2MASS
H (mag)	8.920 ± 0.042	2MASS
K_s (mag)	8.890 ± 0.022	2MASS
W1 (mag)	8.828 ± 0.023	WISE
W2 (mag)	8.897 ± 0.020	WISE
W3 (mag)	8.819 ± 0.031	WISE
$T_{\rm eff}$ (K)	5513 ± 51	ZASPE
$\log g$ (dex)	4.032 ± 0.015	ZASPE
[Fe/H] (dex)	0.26 ± 0.03	ZASPE
$v \sin i$ (km s^{-1})	3.70 ± 0.17	ZASPE
$M_\star$ ($M_\odot$)	$1.104^{+0.020}_{-0.018}$	ZASPE + GAIA + YY
$R_\star$ ($R_\odot$)	$1.669^{+0.022}_{-0.021}$	ZASPE + GAIA
$\rho_\star$ (g cm^{-3})	$0.334^{+0.011}_{-0.012}$	ZASPE + GAIA
$\rho_\star$ (g cm^{-3})	0.28 ± 0.06	exonailer
$L_\star$ ($L_\odot$)	$2.32^{+0.12}_{-0.11}$	ZASPE + GAIA + YY
Age (Gyr)	$8.51^{+0.53}_{-0.48}$	ZASPE + GAIA + YY
A_V	$0.030^{+0.017}_{-0.017}$	ZASPE + GAIA

determination of the transit parameters, we considered the limb-darkening coefficients as additional free parameters in the transit modelling (Espinoza & Jordán 2015), where the limb-darkening law to use is decided following Espinoza & Jordán (2016); in our case, we select the quadratic limb-darkening law. The limb-darkening coefficients were fit using the uninformative sampling technique of Kipping (2013). As described in Espinoza et al. (2016), we also include a photometric jitter parameter, which allow us to have an estimation of the level of stellar noise in the light curves. As for the radial velocities, they are modelled with the `rad-vel` package (Fulton et al. 2018), where we consider a different systemic velocity and jitter factor for the data of each spectrograph. In addition, we also used the stellar density derived in our stellar modelling as an extra 'data point' in our global fit, with the idea being that, given $\mathbf{y} = \{\mathbf{y}_{tr}, \mathbf{y}_{rv}, \mathbf{y}_{\rho_*}\}$ is the data vector containing the transit data $\mathbf{y}_{tr}$, the radial-velocity data $\mathbf{y}_{rv}$ and the stellar density 'data' (obtained form our stellar analysis using GAIA + Isochrones) $\mathbf{y}_{\rho_*}$, because the three pieces of data are independent, the likelihood can be decomposed as $p(\mathbf{y}|\theta) = p(\mathbf{y}_{tr}|\theta)p(\mathbf{y}_{rv}|\theta)p(\mathbf{y}_{\rho_*}|\theta)$. The latter term is assumed to be Gaussian, and is given by

$$p(\mathbf{y}_{\rho_*}|\theta) = \frac{1}{\sqrt{2\pi\sigma^2_{\rho_*}}} \exp - \frac{(\rho_* - \rho^m_*)^2}{2\sigma^2_{\rho_*}},$$

where

$$\rho^m_* = \frac{3\pi}{GP^2}\left(\frac{a}{R_*}\right)^3$$

by Kepler's law, and ρ_* and σ_{ρ_*} are the mean stellar density and its standard deviation, respectively, derived from our stellar analysis. In essence, because the period P is tightly constrained by the observed periodic transits, this extra term puts a strong constraint on a/R_*, which in turn helps to extract information about the eccentricity e and argument of periastron ω from the duration of the transit. This methodology has been updated in `exonailer`. Both an eccentric and a circular model were considered, but the eccentric model was the one favoured by the data (the Bayesian information criterium in favour of the latter model with ΔBIC = 5.4). Just as an additional cross-validation test, we also performed the `exonailer` analysis without using the stellar density value derived from the stellar modelling of Section 3.1. In this case, we obtained a posterior value for the stellar density of 0.28 ± 0.06 g cm^{-3}, which is fully consistent with the value that was estimated with the stellar analysis.

The adopted priors and obtained posteriors of our modelling are presented in Table 3. Figs 6 and 7 show the adopted solution for the transit and orbital variation of K2-161b as a function of the orbital phase, generated from the posterior distributions. The corresponding data is also presented in this plot. We combined the inferred stellar physical properties of K2-161 with the obtained transit and orbital parameters to obtain the physical parameters of the planet. We found that the mass of K2-161b lies in the super-Neptune regime ($M_P = 0.179 \pm 0.021\,M_J$) while its radius is slightly larger than the one of Saturn ($R_P = 0.840 \pm 0.011\,R_J$). These values imply a relatively low bulk density of $\rho_P = 0.37 \pm 0.05$ g cm^{-3}. Additionally, due to its moderately long orbital period the nominal equilibrium temperature of K2-161b is of $T_{\rm eq} = 1065 \pm 12$ K. However, due to the high eccentricity of the system ($e = 0.42 \pm 0.03$), the atmospheric temperature of K2-161b could be significantly different depending on the atmospheric circulation properties of the planet.

3.3 Rotational modulation and search of additional transits

The data with masked transits were used in order to search for rotational modulations from the star and/or the planet, as well as further possible transits and/or secondary eclipses in the data. The detrended data did not show any indication of secondary eclipses, which was expected as the secondary eclipse depth is, at maximum, of order $(R_P/r)^2 = 15.56 \pm 0.6$ ppm if only a reflected light component is considered, which is five times below the attained noise level in the K2 photometry. In this computation, r corresponds to the star–planet separation at the time of the secondary transit as predicted using the values of the orbital parameters found in the global modelling. As for further transits, a BLS on the data reveals two prominent peaks at $P = 0.81$ and $P = 7.39$ d, yet no clear transit signature at those periods is observed. The detrended data did not show additional signals that could be associated to phase curve variations, but any such signal could have been absorbed after the detrending process. No rotational modulation signatures were detected in the photometry.

4 DISCUSSION

4.1 Structure

Fig. 8 displays the full population of well-characterized transiting planets where the super-Neptune region is highlighted in green. K2-161b joins this sparsely populated group of systems having masses in the $0.054\,M_J < M_P < 0.18\,M_J$ range. According to TEPcat (Southworth 2011), there are another 25 systems in this region of the parameter space with radii and masses measured at the 25 per cent level. Among these systems, K2-161b shares similar structural properties to HATS-8b (Bayliss et al. 2015), WASP-107b

Table 3. Transit, orbital, and physical parameters of K2-161b. On the priors, $N(\mu, \sigma)$ stands for a normal distribution with mean μ and standard deviation σ, $U(a, b)$ stands for a uniform distribution between a and b, and $J(a, b)$ stands for a Jeffrey's prior defined between a and b.

Parameter	Prior	Value
Light-curve parameters		
P (d)	$N(11.633\,62, 0.01)$	$11.633\,65 \pm 0.000\,10$
T_0 (d)	$N(2\,457\,906.84, 0.01)$	$2\,457\,906.839\,57 \pm 0.000\,49$
$R_P/R_\star$	$U(0.001, 0.5)$	$0.05178^{+0.0006}_{-0.0005}$
$a/R_\star$	$U(1, 30)$	$13.38^{+0.16}_{-0.18}$
i	$U(0, 90)$	$89.20^{+0.57}_{-0.68}$
q_1	$U(0, 1)$	$0.48^{+0.11}_{-0.09}$
q_2	$U(0, 1)$	$0.36^{+0.08}_{-0.07}$
σ_w (ppm)	$J(10, 5000)$	$79.03^{+0.99}_{-0.95}$
RV parameters		
K (m s^{-1})	$N(0, 100)$	$16.6^{+1.9}_{-1.9}$
e	$U(0, 1)$	0.42 ± 0.03
ω (deg)	$U(0, 360)$	$147.0^{+5.9}_{-6.3}$
$\gamma_{\rm coralie}$ (m s^{-1})	$N(3300, 100)$	$3328.1^{+6.1}_{-5.9}$
$\gamma_{\rm feros}$ (m s^{-1})	$N(3300, 100)$	$3319.9^{+1.3}_{-1.4}$
$\gamma_{\rm harps}$ (m s^{-1})	$N(3300, 100)$	$3341.7^{+1.4}_{-1.5}$
$\sigma_{\rm coralie}$ (m s^{-1})	$J(10^{-2}, 10)$	$0.7^{0.8}_{-0.8}$
$\sigma_{\rm feros}$ (m s^{-1})	$J(10^{-2}, 10)$	$1.7^{+2.8}_{-0.9}$
$\sigma_{\rm harps}$ (m s^{-1})	$J(10^{-2}, 10)$	$2.2^{+2.1}_{-1.1}$
Derived parameters		
M_P (M_J)	–	0.179 ± 0.020
R_P (R_J)	–	0.840 ± 0.011
$\langle T_{\rm eq} \rangle^a$ (K)	–	1054^{+12}_{-15}
a (au)	–	$0.10376^{+0.00043}_{-0.00051}$
ρ_P (g cm^{-3})	–	0.37 ± 0.05

Note. [a]Time averaged equilibrium temperature using equation (16) of Méndez & Rivera-Valentín (2017) with $A = 0$ and $\beta = 1$.

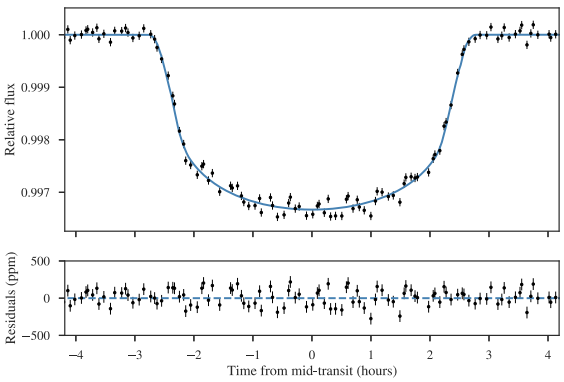

Figure 6. The top panel shows the phase folded Kepler *K*2 photometry (black points) for the K2-161 system around the transit, and the model generated with the derived parameters of EXONAILER (blue line). The bottom panel shows the corresponding residuals.

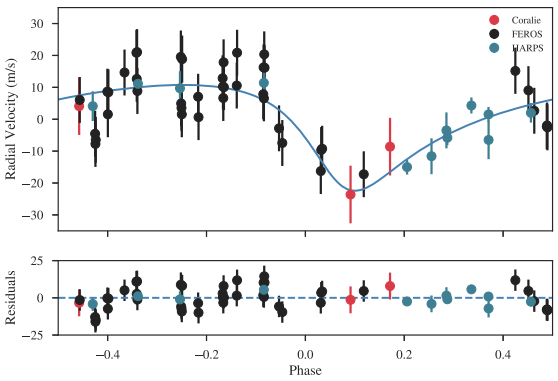

Figure 7. The top panel presents the radial velocities (coloured circles) obtained with the three spectrographs as a function of the orbital phase. The RV model with the derived orbital parameters for K2-161b corresponds to the blue solid line. The bottom panel shows the residuals obtained for these radial velocity measurements.

(Anderson et al. 2017), and WASP-139b (Hellier et al. 2017). These four systems have particularly low densities.

A clear property of the super-Neptune population is that it covers a wide range of internal structures, as can be identified from the different values that the radii can take. In the case of low irradiated planets ($T_{\rm eq} < 1000$ K; Kovács et al. 2010), the radius is mostly set by the amount of solid material in the interior. In this context, K2-161b and the other low density, low irradiation gaseous planets seem to be depleted in solid material when compared to the rest of the population. Specifically, Thorngren et al. (2016) inferred the amount of solid material for some of these planets, finding that the fraction of solids for WASP-139b is consistent with 40 per cent, while the more compact systems (GJ436b, HAT-P-11b, K2-27b) tend to have values between 70 per cent and 90 per cent. K2-161 and the host stars of the other low-density Neptunes do not seem

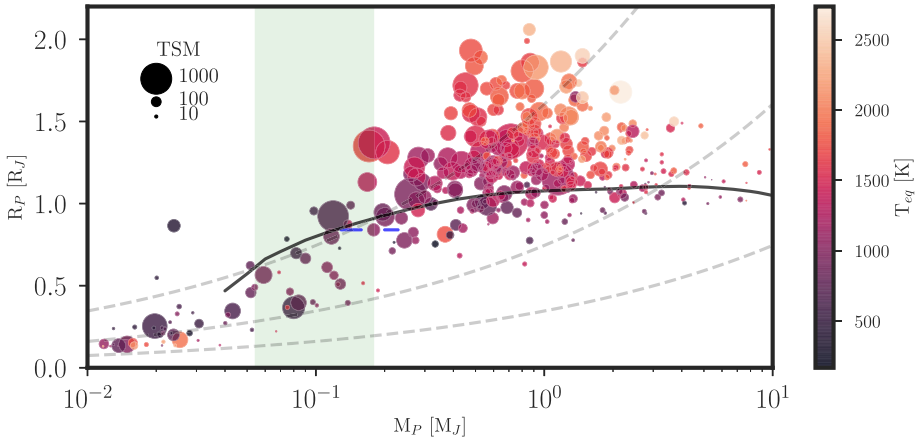

Figure 8. Mass–radius diagram for the population of transiting planets with masses and radii measured with a precision better than 25 per cent. The points are colour coded according to their equilibrium temperature. The size of the points scales with the transmission spectroscopy metric as defined by (Kempton et al. 2018). The continuous black line corresponds to the theoretical radius of the Fortney, Marley & Barnes (2007) models for a core mass of 10 $M_\oplus$ and a similar insolation than K2-161b. The dashed lines correspond to different iso-density curves of 0.3, 3, and 30 g cm^{-3}, from top to bottom. The super-Neptune region, which corresponds to the ice–gas transition of giant planets is highlighted in green. K2-161b (blue errorbars) falls in the region of moderately irradiated low-density super-Neptunes and its structure would be consistent to that of a 10 $M_\oplus$ ice–rocky core of surrounded by a solar metallicity envelope.

particularly metal poor ($0.0 < [Fe/H] < 0.3$), which could be linked to a protoplanetary disc with a low concentration of solids. Therefore, the small gas-to-solids ratio in the envelope of these low-density planets could be produced by their formation and accretion history.

Even though low-mass gaseous planets show a wide variety of structures and fraction of metals, they might share a similar formation mechanism, in which the embryo does not quite enter into the process of run away accretion of the gaseous envelope because it does not reach the pebble isolation mass (e.g. Ida, Guillot & Morbidelli 2016). None the less, these conditions can be satisfied at different regions of the protoplanetary disc. For example, Bitsch, Lambrechts & Johansen (2015) demonstrated that ice giants can be formed at very large orbital distances (40 au) but also inside 5 au, while gas giants form in the region in between. The information about the metal content could be an additional variable that further constrains the location where the planet accretes most of its envelope. In this context, the measurement of the atmospheric metallicities and C/O ratios for these planets is highly valuable, because this value can be used to constrain the region where the planet accreted most of its envelope (Mordasini et al. 2016; Espinoza et al. 2017b). The measurement of the atmospheric C/O ratios is possible through transmission spectroscopy, and has been successfully obtained for the low-density super-Neptune WASP-107b using HST/WFC3 (Kreidberg et al. 2018), where the data is consistent with a sub-solar C/O ratio. K2-161b is a well suited comparison candidate to search for water molecules and constrain the C/O ratio of planets in the ice/gas transition range. Its bright host star, coupled to its low density, translates to a transmission spectroscopy metric (TSM) of 170, which according to (Kempton et al. 2018), puts it in the group of highest priority targets for atmospheric characterization with JWST.

4.2 Orbital evolution

Another particular property of K2-161b besides its low density is the significant eccentricity of its orbit. Fig. 9 shows that K2-161b is among the most eccentric planets having orbital periods shorter than 50 d. In the absence of external mechanisms, the evolution of the orbit of K2-161b should be dominated by tidal interactions produced by the star onto the planet during periastron passages. In this way, K2-161b should circularize its orbit while migrating closer to the star (Jackson, Greenberg & Barnes 2008). As can be also identified in Fig. 9, K2-161b presents one of the shortest circularization time-scales ($\tau_{\rm circ} = 1.7$ Gyr) of the population transiting systems with $P < 50$ d and $e > 0.4$, which is principally caused by the relatively low mass of K2-161b. For example, CoRoT-10b (Bonomo et al. 2010) and HD17156 (Fischer et al. 2007) with a masses of $M_{\rm P} = 2.76 M_{\rm J}$ and $M_{\rm P} = 3.3 M_{\rm J}$, respectively, present circularization time-scales greater than 20 Gyr. Two eccentric systems of this sample that present short circularization time-scales are HAT-P-2b ($M_{\rm P} = 8.87 M_{\rm J}$, $\tau_{\rm circ} = 0.7$ Gyr; Bakos et al. 2007), and HAT-P-34b ($M_{\rm P} = 3.33\,M_{\rm J}$, $\tau_{\rm circ} = 0.3$ Gyr; Bakos et al. 2012). Both systems, however, are significantly younger (~2 Gyr) than K2-161 (8.5 Gyr), which could help in explaining their non-circular orbits.

In order to check if the derived orbital and physical parameters translate in a feasible scenario for the existence of the K2-161b, we studied the tidal evolution history of the system. We used the equations presented in Jackson et al. (2009) that govern the change in a and e as a function of time affected by the tidal interactions produced by the star on the planet and vice versa. We also consider the changes in the radius of the host star as it leaves the main sequence by generating an interpolated evolutionary track from the Yonsei-Yale isochrones. Fig. 10 shows the evolution of a and e for the parameters that we obtained for the K2-161 system, where we assume a tidal quality factor of $Q_\star = 10^6$ (Penev et al. 2018) for the star, and a Jupiter-like $Q_{\rm P} = 3 \times 10^4$ for the planet (Lainey et al. 2009).

We performed several simulations of the tidal evolution by selecting stellar and planetary values from random distributions using the outcomes of our joint modelling. We obtain that K2-161b will be engulfed by its evolving host star before circularizing its orbit in ≈1 Gyr from now. More interestingly, we find that if we go back in time, the planet pericentre distance gets very close to the Roche limit of the system, but does not cross it. For example, when the system was 1 Gyr old, a semi-major axis of $a = 0.175$ au and an eccentricity of $e = 0.85$, translates into a pericentre distance of just 1.4 Roche radii. In this way, one simple origin for the current

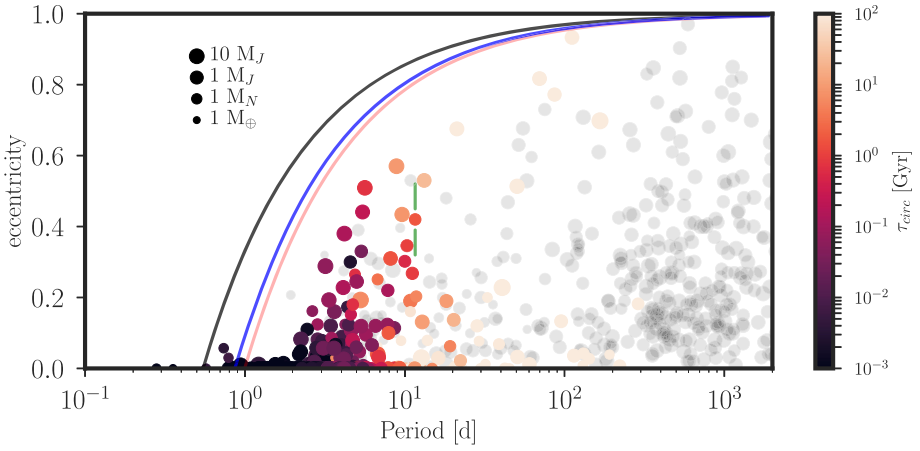

Figure 9. Scatter plot of the eccentricity as a function of the orbital period. Coloured circles correspond to transiting planets where the colour represents the tidal circularization time-scale. The circularization time-scale ($e/(\mathrm{d}e/\mathrm{d}t)$) is obtained by rearranging equation (2) of Jackson, Barnes & Greenberg (2009). The grey circles correspond to non-transiting planets. The size of the circles represents the mass of the object ($M_P \sin i$ in the case of non-transiting planets). K2-161b can be identified as the only system having green error bars. The three solid lines correspond to the maximum eccentricity that an orbit can take such that the periapsis distance lies outside the Roche limit. The red line corresponds to the limit for the physical parameters of the K2-161 system. The blue (black) line corresponds to the limit in the case of a Neptune-like (Jupiter-like) planet orbiting a sun-like star. K2-161b is among the most eccentric systems having $P < 50$ d. Additionally, K2-161b has one of the shortest circularization time-scales among this high eccentricity systems.

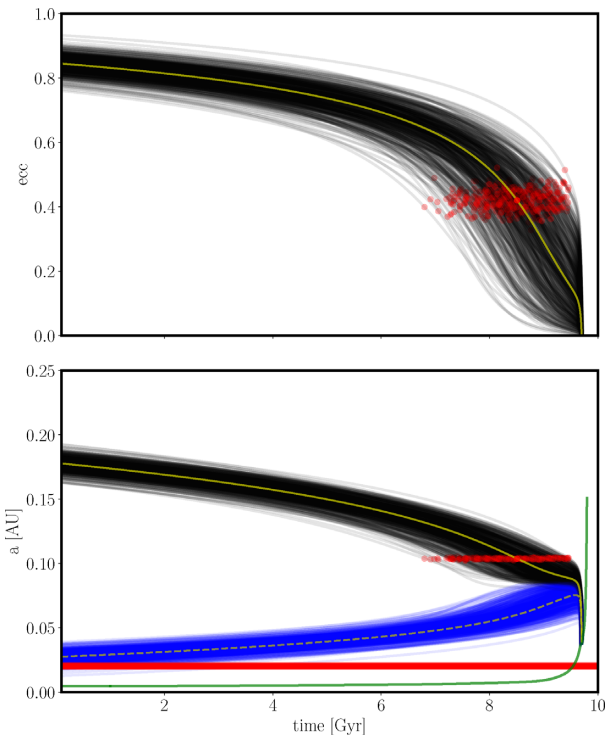

Figure 10. Results obtained for the simulations of the orbital evolution of K2-161b under the influence of the tidal interactions with the star. The top panel corresponds to the eccentricity evolution, where the black yellow line corresponds to the evolution given by the adopted current value of the eccentricity ($e = 0.42$). The middle panel corresponds to the evolution of the semi-major axis (grey lines), periapsis distance (blue lines), Roche limit (red lines), and stellar radius (green line).

parameters of the K2-161 system is that K2-161b could have formed beyond 0.2 au, and then migrated though the proto-planetary disc to ≈0.2 au (e.g. Ida & Lin 2008). As soon as the gaseous disc was dispersed (∼100 Myr), gravitational interactions with additional objects in the system excited the eccentricity of K2-161b to $e \approx 0.9$ (e.g. Beaugé & Nesvorný 2012) and it has been migrating through tidal interactions since then. These results are not sensitive to the adopted value of $Q_\star$, because the planetary tides are significantly stronger than the stellar tides for most of the lifetime of the system.

During the revision process of this paper, we became aware of an independent discovery K2-161b by Johnson et al. (2018). No information about this object, including on analysis and results, was shared between the two teams prior to the submission of either paper.

ACKNOWLEDGEMENTS

RB acknowledges support from FONDECYT Post-doctoral Fellowship Project No. 3180246. AJ acknowledges support from FONDECYT project 1171208, BASAL CATA PFB-06, and project IC120009 'Millennium Institute of Astrophysics (MAS)' of the Millennium Science Initiative, Chilean Ministry of Economy. AZ acknowledges support by CONICYT-PFCHA/Doctorado Nacional-21170536, Chile. MRD acknowledges support by CONICYT-PFCHA/Doctorado Nacional-21140646, Chile. JSJ acknowledges support by FONDECYT project 1161218 and partial support by BASAL CATA PFB-06. Support for CC is provided by Proyecto FONDECYT Iniciación a la Investigación 11150768. This paper includes data collected by the K2 mission. Funding for the K2 mission is provided by the NASA Science Mission directorate. This work has made use of data from the European Space Agency (ESA) mission *Gaia* (https://www.cosmos.esa.int/gaia), processed by the *Gaia* Data Processing and Analysis Consortium (DPAC, https://www.cosmos.esa.int/web/gaia/dpac/consortium). Funding for the DPAC has been provided by national institutions, in particular the institutions participating in the *Gaia* Multilateral Agreement. Based on observations collected at the European Organisation for

Astronomical Research in the Southern Hemisphere under ESO programmes 094.C-0428(A), 0101.C-0407(A), 0101.C-0497(A).

REFERENCES

Anderson D. R. et al., 2017, A&A, 604, A110
Bakos G. Á. et al., 2007, ApJ, 670, 826
Bakos G. Á. et al., 2010, ApJ, 710, 1724
Bakos G. Á. et al., 2012, AJ, 144, 19
Bakos G. Á. et al., 2015, ApJ, 813, 111
Baraffe I., Homeier D., Allard F., Chabrier G., 2015, A&A, 577, A42
Baranne A. et al., 1996, A&AS, 119, 373
Barclay T., Pepper J., Quintana E. V., 2018, ApJS, 239, 15
Barragán O. et al., 2016, AJ, 152, 193
Bayliss D. et al., 2015, AJ, 150, 49
Beaugé C., Nesvorný D., 2012, ApJ, 751, 119
Bitsch B., Lambrechts M., Johansen A., 2015, A&A, 582, A112
Bonomo A. S. et al., 2010, A&A, 520, A65
Borucki W. J. et al., 2011, ApJ, 736, 19
Brahm R. et al., 2015, AJ, 150, 33
Brahm R. et al., 2016, PASP, 128, 124402
Brahm R. et al., 2018a, AJ, 155, 112
Brahm R. et al., 2018b, MNRAS, 477, 2572
Brahm R., Jordán A., Espinoza N., 2017a, PASP, 129, 034002
Brahm R., Jordán A., Hartman J., Bakos G., 2017b, MNRAS, 467, 971
Buchhave L. A. et al., 2012, Nature, 486, 375
Cersullo F., Wildi F., Chazelas B., Pepe F., 2017, A&A, 601, A102
Ciardi D. R., Beichman C. A., Horch E. P., Howell S. B., 2015, ApJ, 805, 16
Dawson R. I., Murray-Clay R. A., 2013, ApJ, 767, L24
Demangeon O. D. S. et al., 2018, A&A, 610, A63
Dressing C. D. et al., 2018, AJ, 156, 16
Espinoza N. et al., 2016, ApJ, 830, 43
Espinoza N. et al., 2017a, MNRAS, 471, 4374
Espinoza N., Jordán A., 2015, MNRAS, 450, 1879
Espinoza N., Jordán A., 2016, MNRAS, 457, 3573
Espinoza N., Fortney J. J., Miguel Y., Thorngren D., Murray-Clay R., 2017b, ApJ, 838, L9
Fischer D. A. et al., 2007, ApJ, 669, 1336
Foreman-Mackey D., Hogg D. W., Lang D., Goodman J., 2013, PASP, 125, 306
Fortney J. J., Marley M. S., Barnes J. W., 2007, ApJ, 659, 1661
Fulton B. J. et al., 2017, AJ, 154, 109
Fulton B. J., Petigura E. A., Blunt S., Sinukoff E., 2018, PASP, 130, 044504
Gaia Collaboration et al. 2018, A&A, 22
Giles H. A. C. et al., 2018, MNRAS, 475, 1809
Hellier C. et al., 2017, MNRAS, 465, 3693
Howell S. B. et al., 2014, PASP, 126, 398
Ida S., Lin D. N. C., 2004, ApJ, 604, 388
Ida S., Lin D. N. C., 2008, ApJ, 673, 487
Ida S., Guillot T., Morbidelli A., 2016, A&A, 591, A72
Jackson B., Greenberg R., Barnes R., 2008, ApJ, 678, 1396
Jackson B., Barnes R., Greenberg R., 2009, ApJ, 698, 1357
Jenkins J. S. et al., 2017, MNRAS, 466, 443
Johnson M. C. et al., 2018, MNRAS, 481, 596
Jones M. I. et al., 2017, A&A, 613, 9
Jordán A. et al., 2014, AJ, 148, 29
Kaufer A., Stahl O., Tubbesing S., Nørregaard P., Avila G., Francois P., Pasquini L., Pizzella A., 1999, The Messenger, 95, 8
Kempton E. M.-R. et al., 2018, PASP, 130, 114401
Kipping D. M., 2010, MNRAS, 408, 1758
Kipping D. M., 2013, MNRAS, 435, 2152
Kovács G. et al., 2010, ApJ, 724, 866
Kovács G., Zucker S., Mazeh T., 2002, A&A, 391, 369
Kreidberg L., 2015, PASP, 127, 1161
Kreidberg L., Line M. R., Thorngren D., Morley C. V., Stevenson K. B., 2018, ApJ, 858, L6
Lainey V., Arlot J.-E., Karatekin Ö., van Hoolst T., 2009, Nature, 459, 957
Luger R., Agol E., Kruse E., Barnes R., Becker A., Foreman-Mackey D., Deming D., 2016, AJ, 152, 100
Luger R., Kruse E., Foreman-Mackey D., Agol E., Saunders N., 2017, AJ, 156, 21
Mayor M. et al., 2003, The Messenger, 114, 20
Méndez A., Rivera-Valentín E. G., 2017, ApJ, 837, L1
Mordasini C., Alibert Y., Benz W., 2009, A&A, 501, 1139
Mordasini C., van Boekel R., Mollière P., Henning T., Benneke B., 2016, ApJ, 832, 41
Penev K., Bouma L. G., Winn J. N., Hartman J. D., 2018, AJ, 155, 165
Petrovich C., Tremaine S., 2016, ApJ, 829, 132
Queloz D., Mayor M., Naef D., Santos N., Udry S., Burnet M., Confino B., 2000, in Bergeron J., Renzini A., eds, From Extrasolar Planets to Cosmology: The VLT Opening Symposium, Springer-Verlag, Berlin, p. 548
Ricker G. R. et al., 2015, J. Astron. Telescopes Instrum. Syst., 1, 014003
Soto M. G. et al., 2018, MNRAS, 478, 5356
Soto M. G., Jenkins J. S., 2018, A&A, 615, 28
Southworth J., 2011, MNRAS, 417, 2166
Thorngren D. P., Fortney J. J., Murray-Clay R. A., Lopez E. D., 2016, ApJ, 831, 64
Udry S. et al., 2017, preprint (arXiv:1705.05153)
Van Eylen V. et al., 2016, AJ, 152, 143
Vanzi L. et al., 2018, MNRAS, 477, 5041
Yi S., Demarque P., Kim Y.-C., Lee Y.-W., Ree C. H., Lejeune T., Barnes S., 2001, ApJS, 136, 417

APPENDIX:

Table A1. RV and BIS measurements for K2-161.

BJD (−2400000)	RV (km s^{-1})	σ_{RV} (km s^{-1})	BIS (km s^{-1})	σ_{BIS} (km s^{-1})	Instrument
58145.8228641	3.332 2	0.009 0	− 0.024	0.010	Coralie
58167.7218311	3.335 0	0.007 0	− 0.000	0.009	FEROS
58198.7443322	3.304 5	0.009 0	− 0.017	0.010	Coralie
58171.7144194	3.342 6	0.002 0	− 0.002	0.002	HARPS
58177.7335895	3.338 2	0.005 5	− 0.006	0.007	HARPS
58178.7258003	3.335 2	0.005 9	0.001	0.008	HARPS
58199.6738848	3.319 5	0.009 0	0.003	0.010	Coralie
58211.7074500	3.326 7	0.002 0	0.009	0.002	HARPS
58212.6562454	3.335 9	0.002 0	0.005	0.002	HARPS
58213.6244947	3.343 2	0.002 0	0.006	0.002	HARPS
58214.6231712	3.343 7	0.002 8	0.007	0.004	HARPS
58235.5508853	3.330 1	0.005 5	− 0.006	0.007	HARPS
58236.4894689	3.346 0	0.002 2	0.008	0.003	HARPS
58239.5556333	3.328 5	0.007 0	− 0.006	0.009	FEROS
58239.5677837	3.321 4	0.007 0	− 0.008	0.009	FEROS
58239.5796199	3.328 3	0.007 0	− 0.019	0.009	FEROS
58241.7013063	3.320 5	0.007 0	0.009	0.009	FEROS
58241.6923621	3.326 9	0.007 0	0.001	0.009	FEROS
58242.6012465	3.330 4	0.007 0	− 0.012	0.009	FEROS
58242.6088207	3.340 7	0.007 0	− 0.003	0.009	FEROS
58243.6728970	3.312 4	0.007 0	− 0.004	0.009	FEROS
58243.5960625	3.317 0	0.007 0	0.001	0.010	FEROS
58244.5790597	3.303 6	0.007 0	− 0.009	0.009	FEROS
58244.6109274	3.310 6	0.007 0	− 0.003	0.010	FEROS
58249.6027837	3.322 5	0.007 0	− 0.009	0.010	FEROS
58249.4650452	3.328 9	0.007 4	− 0.025	0.011	FEROS
58250.5395590	3.325 9	0.007 0	− 0.005	0.009	FEROS
58251.5932739	3.334 5	0.007 0	− 0.006	0.009	FEROS
58261.5307685	3.317 6	0.007 0	− 0.015	0.009	FEROS
58261.5458842	3.317 3	0.007 0	0.000	0.009	FEROS
58261.5383175	3.317 9	0.007 0	− 0.020	0.009	FEROS
58262.4795489	3.345 8	0.004 5	− 0.002	0.006	HARPS
58262.5348530	3.315 3	0.007 0	− 0.010	0.009	FEROS
58262.5424179	3.312 1	0.007 0	− 0.018	0.009	FEROS
58262.5499684	3.313 4	0.007 0	− 0.004	0.009	FEROS
58263.5071991	3.340 7	0.007 0	− 0.017	0.009	FEROS
58263.5147548	3.332 5	0.007 0	− 0.010	0.009	FEROS
58263.5222990	3.340 9	0.007 0	− 0.010	0.009	FEROS
58263.5298571	3.328 7	0.007 0	− 0.012	0.009	FEROS
58263.5435131	3.352 8	0.002 0	0.001	0.002	HARPS
58264.5319999	3.351 4	0.005 2	0.006	0.007	HARPS
58264.5525416	3.339 4	0.008 1	0.006	0.012	FEROS
58264.5601077	3.324 8	0.007 0	− 0.014	0.010	FEROS
58264.5676783	3.323 4	0.007 0	− 0.019	0.010	FEROS
58264.5752260	3.321 4	0.007 0	− 0.005	0.011	FEROS
58264.5827913	3.338 7	0.007 2	0.016	0.011	FEROS
58265.5360829	3.332 7	0.007 0	− 0.020	0.010	FEROS
58265.5436332	3.330 1	0.007 0	− 0.011	0.009	FEROS
58265.5511918	3.326 5	0.007 0	− 0.007	0.009	FEROS
58265.5587443	3.337 7	0.007 0	0.003	0.009	FEROS
58265.5663100	3.329 9	0.007 0	− 0.005	0.009	FEROS
58266.4923891	3.327 7	0.007 7	0.015	0.012	FEROS
58266.4999270	3.336 1	0.007 0	− 0.039	0.011	FEROS
58266.5059263	3.353 1	0.004 8	0.007	0.006	HARPS
58266.5074907	3.326 4	0.007 0	− 0.011	0.010	FEROS
58266.5150622	3.340 2	0.007 0	− 0.002	0.010	FEROS
58266.5226106	3.336 0	0.007 0	− 0.012	0.010	FEROS

This paper has been typeset from a TEX/LATEX file prepared by the author.